Quantitative protein sensing with germanium THz-antennas manufactured using CMOS processes

ELENA HARDT,[1,*] CARLOS ALVARADO CHAVARIN,[1]
SOENKE GRUESSING,[2] JULIA FLESCH,[3] OLIVER SKIBITZKI,[1]
DAVIDE SPIRITO,[1] GIAN MARCO VITA,[4] GIOVANNA DE SIMONE,[4]
ALESSANDRA DI MASI,[4] CHANGJIANG YOU,[3]
BERND WITZIGMANN,[5] JACOB PIEHLER,[3]
AND GIOVANNI CAPELLINI[1,4]

[1] *IHP-Leibniz Institut für innovative Mikroelektronik, Im Technologiepark 25, 15236 Frankfurt (Oder), Germany*
[2] *University of Kassel, Wilhelmshoeher Allee 71, 34121 Kassel, Germany*
[3] *Department of Biology/Chemistry and Center for Cellular Nanoanalytics (CellNanOs), University of Osnabrueck, Barbarastr. 11, 49076 Osnabrueck, Germany*
[4] *Department of Sciences, Università Roma Tre, Viale G. Marconi 446, 00146, Roma, Italy*
[5] *Friedrich-Alexander Universität Erlangen-Nürnberg, Konrad-Zuse Str. 3/5, 91052 Erlangen, Germany*
*hardt@ihp-microelectronics.com

Abstract: The development of a CMOS manufactured THz sensing platform could enable the integration of state-of-the-art sensing principles with the mixed signal electronics ecosystem in small footprint, low-cost devices. To this aim, in this work we demonstrate a label-free protein sensing platform using highly doped germanium plasmonic antennas realized on Si and SOI substrates and operating in the THz range of the electromagnetic spectrum. The antenna response to different concentrations of BSA shows in both cases a linear response with saturation above 20 mg/mL. Ge antennas on SOI substrates feature a two-fold sensitivity as compared to conventional Si substrates, reaching a value of 6 GHz/(mg/mL), which is four-fold what reported using metal-based metamaterials. We believe that this result could pave the way to a low-cost lab-on-a-chip biosensing platform.

1. Introduction

Recent improvements in the performance of THz devices, such as sources and detectors, have rapidly advanced the field of biosensing [1] and swiftly opened up innovative perspectives in medicine or biomolecular applications. For this reason, THz spectroscopy is now regarded as one of the most sensitive and promising methods for investigating biomolecules and their conformational changes [2–6]. As an example, Liu et. al [7]. studied the suppression of tumor cell proliferation by aspirin using THz sensing, Shangjun Lin et. al [8]. demonstrated the sensitivity of the resonance frequency of the new type of THz Metasurface sensor to the refractive index at 65 GHz/RIU (refractive index unit) with the detection limits for cancer biomarkers carbohydrate antigen 125(CA125) and carbohydrate antigen 199(CA199) at 0.01 U/ml.

One advantage of THz biosensing is the expectation of characteristic fingerprints due to vibration and rotational energies, which corresponds to intra/inter molecular weak hydrogen bonds in various biomolecules, such as in, e.g., proteins [9,10]. This advantage could enable its use in the near future to create a database of disease biomarkers [11,12]. Indeed, diverse serum markers such as circulating nucleic acids, extracellular vesicles (e.g., microvesicles, exosomes), and proteins (e.g., human serum albumin, alpha-fetoprotein, lactate dehydrogenase, and human

chorionic gonadotropin) can be specifically monitored in patients as their concentrations and/or post-translational modification change with the disease onset, progression, or treatment [13,14]. Biosensors represent excellent analytical tools for an effective biomarker detection especially in liquid biopsy, which are obtained in a minimal and non-invasive way through the sampling of body fluids (e.g., blood, plasma, serum, saliva, pleural effusion, urine, and cerebrospinal fluid) [13,15]. Therefore, the early identification of reliable serum molecular biomarker by using biosensor platforms will significantly improve disease prognosis and survival rates and will open the door to global healthcare access [5,16,17].

One of the major hurdles of THz biosensing is the size mismatch existing between the bioanalytes such as HIV-Virus, Proteins and DNA (few nm) and the wavelength of the electromagnetic field (several tens of μm) [9,18]. To overcome this problem, it has been suggested to enhance the THz radiation-bioanalyte interaction by exploiting plasmonic effects [19]. In particular, localized surface plasmon resonances (LSPR) have received substantial attention, thanks to their prior demonstration in the spectral range 200 to 1000cm^{-1} (6 to 30THz) [20]. By inducing LSPR resonance conditions, it is possible to confine the THz radiation into subwavelength volumes. Such confinement results in an electric field intensity orders of magnitude larger within the so-called "hot–spot" regions, thus potentially allowing bioanalyte sensing at very low concentrations.

An effective strategy for detection and monitoring of biomolecules exploits the shift in the LSPR in response to a change of the medium refractive index, due to the presence of molecules on the surface. This can be made selective with proper biofunctionalization. As an example, Lee et. al [21]. observed different types of carbohydrate molecules with high sensitivity (10-100 mg/dL) by using THz sensors based on gold nano-slot antenna arrays. Ahmadivand et. al [22]. have used multimetallic planar plasmonic resonators made of iron and titanium to excite toroidal dipoles in the THz range and quantitatively observe the Zika-virus (ZIKV) envelope protein with the help of a specific ZIKV antibody with a detection limit of ~24 pg/mL. Unfortunately, these very promising results have been obtained using biosensing platforms that cannot be easily manufactured using mass production technology, which is critical for a broad adoption of low-cost applications of THz sensors.

Consequently, complementary metal-oxide-semiconductor (CMOS)-compatible THz technologies are now in the spotlight [23,24], since one could leverage their massive parallel fabrication schemes to obtain biosensors at a very convenient cost. Moreover, CMOS based sensors could be easily connected on-chip to data storage, processing, and/ or communication systems based on mainstream Si-based microelectronics, opening the way to low-cost sensor Systems on Chip. Within this framework, the nowadays CMOS-compatible Ge/Si material system [25] is attracting a growing attention as plasmonic material, particularly since the demonstration that highly n-doped Ge can be designed and structured as a sensing platform to realize THz LSPR conditions, as we have shown in simulations [26] and demonstrated qualitatively by using lipoic acid as analyte [27]. The sensitivity of Silicon-based plasmonic antennas to bacteria layer in particular selective recognition of Gram positive/ negative strains due to their different response THz range [28], can widen the application of the methods here proposed.

In this work, we report on the protein sensing capability of Ge/Si bow-tie antennas arrays operating in the vicinity of 1 THz and manufactured using CMOS processes in an industry-standard Si foundry pilot line. As a model protein we have used the widely accepted bovine serum albumin (BSA), which was incubated and immobilized on the antennas at different concentrations and corresponding thicknesses, as shown by FT-IR spectroscopy and cross sectional Scanning electron microscopy (SEM). The development of reliable albumin-based biosensors, which is carried out in the work on the basis of studying BSA of different concentrations, implies the possibility of rapid monitoring of the presence of bacteria in the organism due to the ability of albumin to recognize and bind toxins [29–32]. By using an optimized antenna design relying on

low losses SOI substrates, we detected resonance spectral shifts as large as 130 GHz in response to BSA layers of a few nm-thickness, with an antenna sensitivity as high as ∼6 GHz/(mg/mL). We point out that this value is 4 times larger than those reported on metal-based metamaterial sensors at different concentration of BSA [4].

2. Methods

2.1. THz antenna fabrication and simulation

The bow-tie antennas is a resonant structure featuring with two trapezoidal arms and a sub-wavelength gap in between, as shown in Fig. 1. The arms consist of highly doped Ge which shows plasmonic properties for electromagnetic THz radiation. Due to the formation of surface plasmons, a THz field enhancement of up 10^4 in the gap and 10^2 at the end of the arms has been calculated [26] (Fig. 1(j)) for excitation with radiation polarized along the axis of the antenna (x-polarization), which leads to a highly sensitive surface sensing mechanism. The antennas were obtained by standard lithographic processes in a 130 nm-SiGe BiCMOS pilot line from ultra-high doped, 1.5 μm-thick Ge heteroepitaxial layers deposited on 200 mm Si(001) (see Figs. 1(a)-(c)) and on 220 nm Si/2 μm SiO₂/Si(001) SOI substrates (see Figs. 1(d)-(f)) by means of an industry-grade reduced pressure chemical vapor deposition reactor. The deposition of Ge was carried out at 350°C using germane for Ge growth and phosphine for the n-type co-doping. The obtained layers are fully relaxed, feature a spatially-homogeneous doping concentration with fully activated ∼1×10^{19} cm^{-3}. The Ge/Si layer was then capped by a 30 nm-thick Si₃N₄ layer and flash annealed at 700°C to improve the material quality and carrier mobility up to 370 cm²/Vs while avoiding dopant out-diffusion. The antennas are then fabricated using photolithography and reactive ion etching. Subsequently, a second 30 nm-thick Si₃N₄ layer is deposited to encapsulate the antennas [26] (see Figs. 1(c), (f), and (g)).
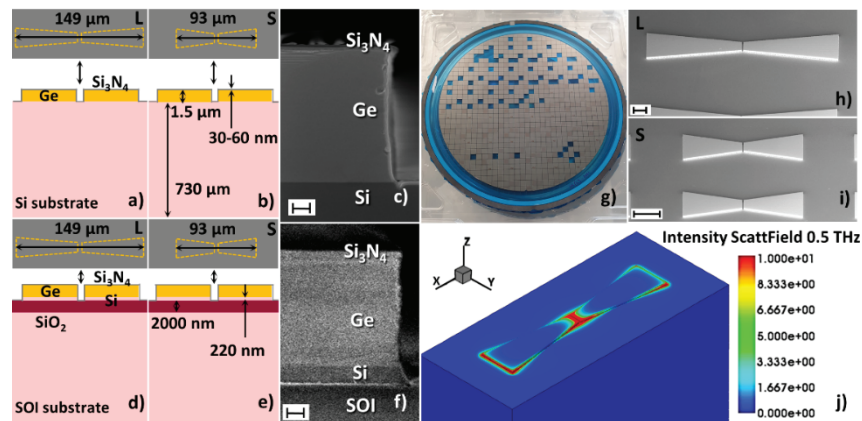
Fig. 1. Sketch and SEM cross section of the Ge antennas on (a)-(c) Si substrate (d)-(f) SOI substrate (scale bars: 200 nm). Photo of the wafer from above (g), each sample corresponds to 6 × 6 mm. SEM images of the Ge-based bow-tie antenna design L (h) (scale bars: 10 μm) and antenna design S (i) (scale bars:20 μm). Model and simulated intensity of scattered field of the antenna design L on SOI substrate at 0.5 THz (j).

Two bow-tie antenna geometry designs were realized on both Si and SOI substrates. The two share the same antenna base width of 30 μm, width at the gap of 10 μm and an antenna gap of 1 μm, while differing in their total length (long axis), which is 149 μm, i.e., 74 μm per antenna (see Figs. 1(a), (d), and (h)) and 93 μm (see Figs. 1(b), (e), and (i)), i.e., 46 μm per antenna for the

designs "Long" (L) and "Short" (S), respectively [33]. The top view SEM image of a typical L and S antennas are shown in Figs. 1(h) and (i), respectively.

The antennas are arranged in a 5×5 mm array of 209 μm lateral pitch (x-axis) for the L design and 133 μm for the S antennas, respectively. Consequently, for the design L we have approx. 53.2 structures/mm^2, while the design S has a density of antennas doubled at 107.4 structures/mm^2. It can be noted that an increase of the number of antennas per mm^2 corresponds clearly to an increase "hot–spot" density, i.e., the antenna gap, where the THz signal field enhancement occurs [33].

Comprehensive finite-element electromagnetic simulations of the antenna array spectral response in the 0.2-1.5 THz range have been made, using the methods and material parameters as described in [26,27,33], taking into account the different substrate composition. As an example, in Fig. 1(j) we report the 3D FEM analysis of an L antenna on SOI by plotting the 0.5 THz electrical field intensity distribution, highlighting the increased field intensity at the antenna gap, i.e., in its hotspot. The field intensity is normalized.

## 2.2. Deposition of BSA biolayers

BSA was used as a model protein for biosensing in this study. BSA is a homolog of human serum albumin (HSA) and is used in pharmacokinetic and affinity tests of drugs as replacements for HSA [14,34] because it is cheaper and easier to obtain [17]. The first albumin studies show that Albumin has the capability to bind a plethora of ligands such as metal ions, drugs, and bacteria toxins render this protein of particular interest as a biosensor. BSA has a 79.8% sequence homology with HSA, and like HSA has a molecular weight of ~66 kDa. It is composed of three domains, and has 17 conserved disulfide bridges that contribute to the high protein stability [34–36]. BSA with ≥98% purity (Merck KGaA, Darmstadt, Germany) was dissolved in ultrapure water (UPW) with 25°C resistivity >18 MΩ·cm as reported previously [37]. We have investigated BSA concentrations ranging from 0 up to 40 mg/mL, which is comparable to the average HSA concentration in the human plasma [37].

All antenna samples used as substrates were cleaned with isopropanol (IPA, ≥99.5% purity, Honeywell) for 5 minutes in an ultrasonic bath to remove any possible organic residues and contaminants, and then dried (see Fig. 2, step I) under N$_2$ flow. The samples were then incubated in the BSA solution for 5 hours on a stir plate (Sustainable Lab Instrument SU1020). In order not to destroy the biolayer, the samples were air-dried for 30-60 minutes after the incubation under a controlled laminar flow hood. Color changes were observed by optical microscopy due to the incubation steps (Fig. 2, step II). The native silicon oxynitride is favoring the adsorption of BSA by the formation of hydrogen bonds on the silicon nitride surface, evenly covering the Ge antennas [37]. In order to remove the BSA biolayers, samples were washed overnight (~18 h) with water on the stir plate [37] (Fig. 2, step III).

After each of the three steps, the THz spectra of each sample at their respective concentration were measured by FT-IR, SEM and THz-TDS techniques.

For reliable comparison, four samples with different substrates and designs (Si: L and S; SOI: L and S) were incubated together in one beaker for each concentration. Each concentration of BSA was repeated three times to generate three nominally identical samples for each of the four combinations of substrate and designs using fresh samples every time. During the incubation, the beakers were covered to prevent contamination and evaporation. All samples were processed and analyzed within one day.

Fourier transform infrared (FT-IR) spectroscopy spectrum analysis is a reliable method to detect the functional groups on the surfaces of the immobilized BSA layers at different concentrations. Native BSA is characterized by an amide I band maximum around 1653 cm^{-1} assigned to the typical α-helix conformation. During the progression of proteolysis process, the conversion of α-helices into unordered structures causes a drastically reduction of the band at 1653 cm^{-1} and
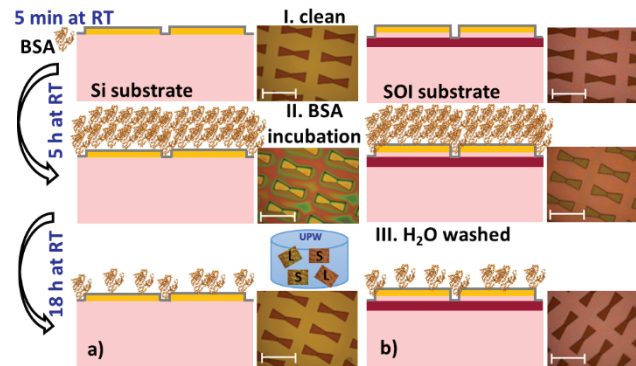
Fig. 2. Procedure for immobilizing BSA (PDM: 4F5S) [35] on Ge-based structures covered with silicon nitride on Si (a) and SOI (b) substrates. Steps Description: (I) To remove chemical contaminants, samples were cleaned with IPA and dried: "*clean*". (II) The antennas were incubated in a BSA solution (c= 2.5, 5, 10, 20 and 40 mg/mL) for 5 hours at room temperature. The BSA protein was immobilized on the antennas and dried after the step. (III) Wash with ultrapure water overnight at room temperature to remove excess BSA: "*washed*". Thereafter, the samples were dried. The optical microscopy images show the top view of design S at 50x magnification (scale bars: 100 μm).

an increase in the concentration of free carboxylates COO^- groups (absorption of 1593 and 1402 cm^{-1}) [38]. We used FT-IR as an auxiliary method to confirm the presence of the albumin on the samples and compared the results to the values stated in the literature [39,40], using a Bruker FT-IR Vertex 80v under vacuum featuring a spectral resolution of 4 cm^{-1}.

Figure 3 shows an average of two samples with BSA at concentrations of 2.5, 10 and 20 mg/mL and without BSA ("clean") in the wavenumber range from 1000 to 1800 cm^{-1} (30 to 54 THz), using the vacuum signal as a reference.

The samples on the Si substrate without BSA immobilization ("*clean*") only show a Si-O-Si transmission dip at 1107 cm^{-1}. Thereby the clean samples on the SOI substrate showed more intense and thicker Si-O-Si dip in the range of 1100-1200 cm^{-1}, due to the additional 2 μm-thick SiO_2 layer (see Fig. 3(b)).

The FT-IR spectra of the BSA samples are a combination of the characteristic absorption bands of the protein. The spectral feature observed in the 1500-1700 cm^{-1} range can be assigned to the amino acid side groups [41]. In particular, the vibrational modes of the peptide backbone generate amide I and II bands. We can see the amide-I dips with the $C = O$ stretching vibration (1658 cm^{-1}) and amide-II dips with the C-N stretching vibration and N-H bending vibration (1541 cm^{-1}) [39,40]. The bands at 1400 cm^{-1} and 1450 cm^{-1} (encircled in Figs. 3(a) and (b)) are attributable to asymmetric and symmetric methyl bending and to COO^- groups [41].

For increasing albumin concentrations, we observed a continuous decrease of the transmission, as we can see in Fig. 3, which we will show is linked to an increased thickness of the BSA adsorbed layer. This in turns, indicates a homogeneous BSA distribution, and can be compared with the experimental FT-IR spectra of BSA of different concentrations in [42] with no linear dependence due to the inhomogeneous BSA distributions.

To thoroughly confirm the presence of the biolayer and its distribution on the antenna/substrate-surfaces, the BSA layer thickness (cross-section) was characterized using a scanning electron microscope (SEM) using a 1.5 kV electron beam at 0° to the surface of the sample. Figure 4 presents the comparison between thickness of BSA layer by concentration 2.5, 10 and 20 mg/mL for Si substrate (Figs. 4(a)–(c)) and for SOI substrate (Figs. 4(d)–(f)). For each SEM image, a specific sample was prepared using the BSA process (up to step II, Fig. 2 and Sect. 2.2).
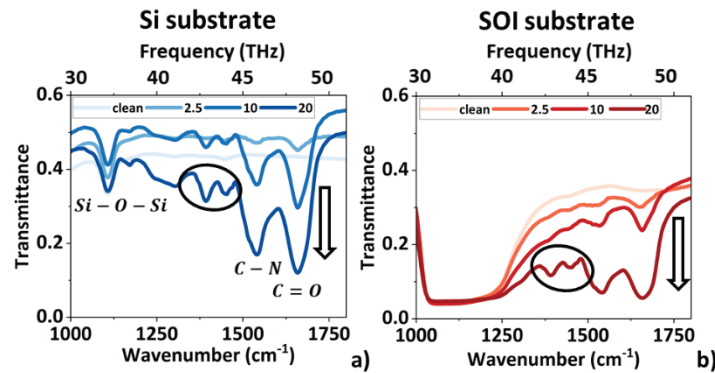
Fig. 3. Detection of the different concentration of a BSA layer on Si (a) and SOI (b) substrates in FT-IR.

As shown in Fig. 4 the thickness of the BSA on the substrate is at least twice that on the top of the antenna. Although BSA is observed to dry not homogeneously on the surface, we can see a general trend of higher thickness on the substrate at higher BSA concentration for both substrates (see Fig. 4 and Table 1).
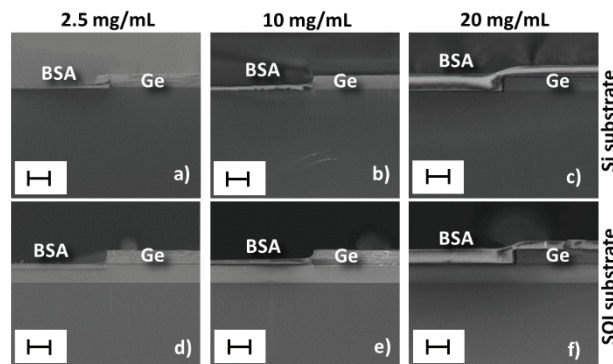
Fig. 4. SEM side view of Si (a)-(c) and SOI (d)-(f) substrates with different BSA concentrations (2.5, 10 and 20 mg/mL). Focus on the substrate and antenna. Scale bars: 2 μm.

Table 1. The different concentrations result in different thickness of the BSA layer after incubation

BSA concentration (mg/mL)	Thickness of BSA layer on the substrate
2.5	~30-50 nm
10	~280-380 nm
20	~1.7-2.2 μm

2.3. THz-TDS analysis

The spectral response of the Ge antennas was studied by Terahertz time-domain spectroscopy (THz-TDS) in transmission mode using a TERASMART tool from Menlo GmbH in the frequency range $f = 0.2\text{-}5$ THz with a resolution of 1.2 GHz, using a linearly polarized source. The

Fabry-Perot contribution to the signal arising from the ~700 μm-thick substrate was removed by suppression of the corresponding echo in the time-domain data using Teralyzer software (Menlo GmbH). A standard THz-TDS spectroscopy setup is shown in Fig. 5(a). You can also find the THz-Time Domain Spectroscopy System in an extended form in [16] and [43,44].

The spectral response of the antenna was obtained from the transmission ratio $E_{ON}(f)/E_{OFF}(f)$ between the electrical field $E_{ON}(f)$, measured with the source polarization vector aligned along the long (active) antenna axis (x-axis) and the electrical field $E_{OFF}(f)$, that is instead measured when the polarization axis is set orthogonal to the long axis (y-axis). The measurement signal in the inactive state $E_{OFF}(f)$ corresponds to the measurement signal from a silicon chip of the same thickness. To avoid misalignment due to replacing the sample with the Si chip, we have therefore taken a more accurate reference by rotating the sample by 90 degrees.

The measured absorption coefficient $\alpha(f)$ was obtained from the following relationship:

$$\alpha(f) = -\frac{2}{d} \ln \left[E_{ON}(f)/E_{OFF}(f) \frac{(n(f)+1)^2}{4n(f)} \right] \tag{1}$$

where $n(f) = 1 + \frac{c}{2\pi v d}\phi(f)$ is the refractive index, d the sample thickness, and $\phi(f) = \phi_{ON}(f) - \phi_{OFF}(f)$ is the phase shift existing between the *ON* and *OFF* electrical fields [44].

The results comprised an average of 100 accumulated spectra per sample for each *ON* and *OFF* electrical field orientation, with each sample measurement lasting less than 2 minutes. The THz optics focalize the beam to a size of about 1 mm, thus only a smaller area of the whole sample is illuminated, which corresponds to activating ~53 antennas for design L and ~107 for design S. For the precise measurement, the samples are not taken out during the *ON* and *OFF* position and only rotated within the sample holder.

3. Results and discussion

We now start our discussion with the characterization of the "*clean*" antennas, i.e., prior to their functionalization with BSA, and the comparison between experimental results and simulations. Figures 5(b) and 5(c) show the spectral measurements of the absorption coefficient α (solid lines) together with their relative theoretical absorption (dashed lines) curves expressed as dichroic ratio $DR = -\log[E_{ON}(f)/E_{OFF}(f)]$ for L and S design antennas, respectively, realized on Si (blue) or SOI (red) substrates.

In all of the four implementations, we can see clear resonance peaks centered at $f_0 = 0.75$-0.85 THz for the L-antennas, and at $f_0 = 1.1$-1.2 THz for the S-antennas. The presence of the 2 μm oxide layer in the SOI substrate induces an increase of approximately 0.1 THz of the resonance frequency. The SOI also induces a substantial narrowing of the spectral absorption, which increase to $Q = f_0/FWHM$ ~2.6 from the value of ~1.9 obtained for antennas on Si (the values of f_0 und $FWHM$ = full-width at half-maximum have been obtained by a Lorentzian fit). We notice that the *Q*-factor increase comes without loss of the absorbance. This improvement is attributed to the reduction of the radiative losses brought about by the higher resistivity SOI substrate.

We observe a shift between experimental and simulated experimentally observed absorption frequency f_0 of ~0.1 THz, that is mainly due to collective response of the antenna arrays [26]. Indeed, while simulations are based on infinitely wide arrays owing to the boundary conditions, in the experimental data, only a finite number of antennas is illuminated, as reported in Sect. 2.3. As a result, the array effect cannot match exactly the experiments. In addition, we cannot rule out that there are possible deviations in the material properties of the antennas (doped Ge), the substrate (Si) and the oxide (SiO_2) from what measured on average. This could lead to the observed discrepancy of ~0.1 THz between the measured and calculated f_0.

In Fig. 5(d) we calculate the intensity field enhancement within the antenna gap for the L- and S-antennas on both Si and SOI substrates. In the spectral range of the L-antennas resonance (f_0~0.8 THz), the SOI substrate promote a twofold gap field enhancement, as compared to

antennas of the same design realized on bare Si. The same improvement is also observed for the S-antennas in their resonance range of $f_0 \sim 1.1$ THz.
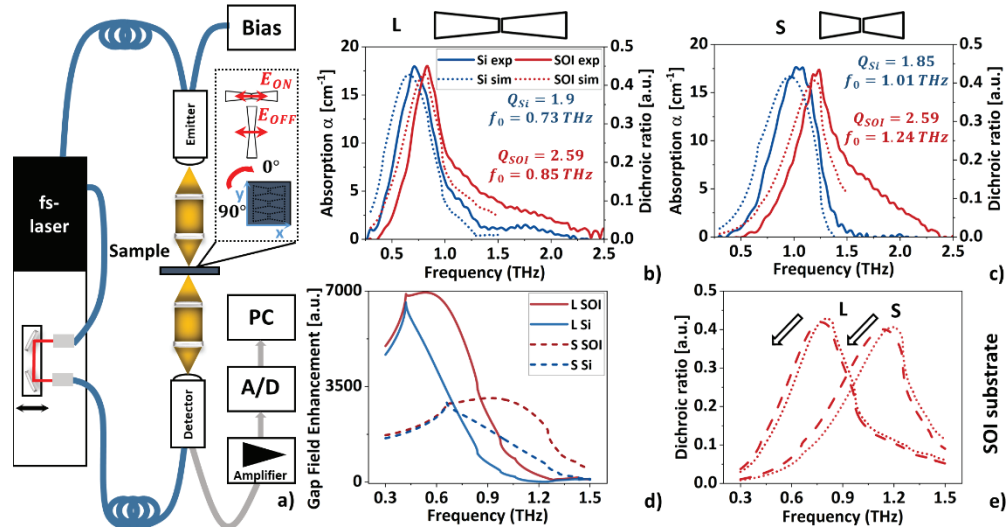

Fig. 5. Schematic representation of the setup for the TDS-THz spectroscopy (according to [44]) (a). Comparison of Si (blue) and SOI (red) substrate effect on the resonance of (b) design L and (c) design S. Solid line: experimental results of absorption. Dashed line: related simulations shown as D.R. Comparison of simulation results of the gap field enhancement of design L (solid line) and design S (short dash line) on Si substrate (blue) and SOI substrate (red) (d). The simulation for L and S with BSA layer (long dashed line) and without BSA layer (short dashed line) for SOI substrate (e).

To show the effect of the deposition of a protein layer on the antennas and to introduce the expected sensing mechanism, in Fig. 5(e) we show the simulated effect on the antenna resonance brought about a gap-filling layer of BSA, for both antenna designs (L and S) on SOI substrate. In the simulation, we described the protein layer with a real-valued refractive index n(BSA) = 1.59 (similar to [45]), which results in good agreement between experiment and simulation. As compared to the clean antennas (short dashed line), the BSA-functionalized ones (long dashed lines) show a red shift of the resonance, i.e., $-\Delta f_0 \sim 26$ GHz for the L design and $-\Delta f_0 \sim 48$ GHz for the S design.

In Fig. 6 we can see the experimental results of THz spectroscopy to Ge antennas at different BSA concentrations. As the BSA concentration increases from 0 ("*clean*") to 40 mg/mL the resonance curve continuously shifts to lower frequencies for both substrates and designs, the darker the curve color, the higher the BSA concentration. Interestingly, after the removal of the BSA layer through washing, the resonance frequency returns approximately to that of the corresponding clean antenna sample, with a difference of resonance between "*clean*" and "*washed*" sample of ~1-5 GHz. This shift, close to our spectral resolution of 1.2 GHz, may be due to residues of BSA remaining on the antenna surface after the water washing process [37].

In Figs. 6(b), 6(d), 6(f), and 6(h) we show the extracted data as a box plot diagram for antenna designs L and S on Si and SOI substrates as a function of the BSA concentration. They are an average of three samples for each of BSA concentrations and of 15 samples for "*clean*" and "*washed*" conditions. This implies that during this study we have measured 45 chiplets extracted from two 200 mm wafers (Si and SOI substrates), that have shown high repeatability and have been produced at a low-cost/high throughput thanks to the qualified CMOS process in their manufacturing.
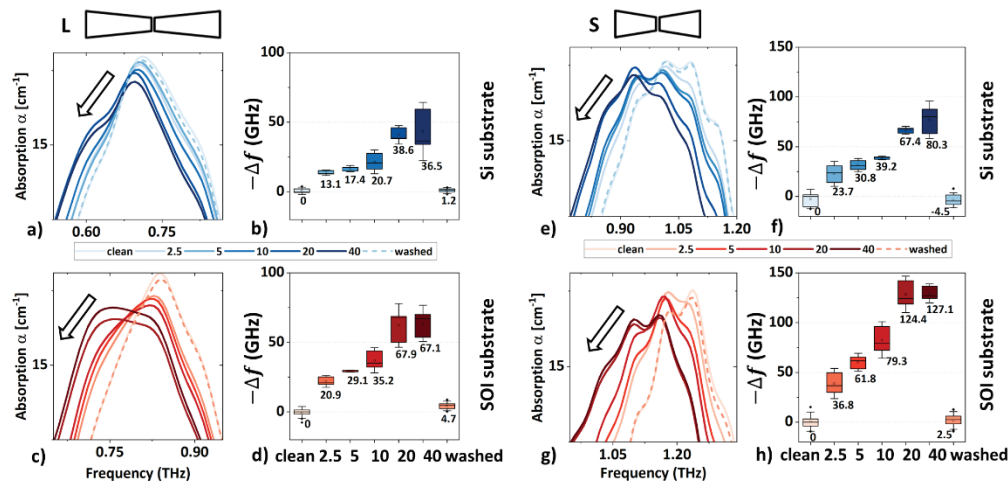
Fig. 6. Sensitivity of Ge antennas on Si (a), (b) and SOI (c), (d) substrates for design L and on Si (e), (f) and SOI (g), (h) substrates for design S to the presence of an albumin layer of different concentrations. Removal of the albumin layer ("*washed*" state) returns the resonance shift to the initial level ("*clean*" sample).

We can observe that the resonance shifts almost linearly for increasing concentration up to the saturating concentration of 20 mg/mL, probably because the BSA layer beyond that limit is so thick that it completely fills the hot-spot gap and becomes undistinguishable from the 40 mg/mL one (see Sect. 2.2). We notice also that the SOI-based samples (see Figs. 6(d) and 6(h)) present the larger shifts compared to Si-based samples (see Figs. 6(b) and 6(f) for all concentrations used in this work). This correlates with the improvement of gap field enhancement using SOI substrates (Fig. 5(d)). The boxplot analysis also shows an evident saturation of sensitivity at the highest concentration, which may indicate the unsuitability of the method for detecting concentrations of biomolecules above 20 mg/mL. This can be understood by the complete coverage of the antenna gap height by the BSA layer at 20 mg/mL (Figs. 4(c) and 4(f)), rendering the hot-spots unable to sense further variations.

The rate of change of the resonant frequency defined as the resonance shift as a function of BSA concentration $|\Delta f_0|/$(mg/mL) was calculated for the four configurations. The sensitivity of Ge-based antennas on Si substrate are ~1.7 GHz/(mg/mL) and ~3 GHz/(mg/mL) and on SOI substrate ~3 GHz/(mg/mL) and ~6 GHz/(mg/mL) for design L and S, respectively. We can see that S-antennas have twice the sensitivity as compared to L-antennas, for the same substrate. This confirms the simulations, given the S design features a twice larger resonance shift for the same BSA coverage (see Fig. 5(e)).

In comparison, Wang et al [4]. followed BSA concentrations using metal-based metamaterials biosensors, reporting a sensitivity of ~95 GHz/(mmol/L) which corresponds to ~1.4 GHz/(mg/mL). This represents a four-fold increase in sensitivity of our semiconductor-based plasmonic platform.

We notice that we were able to detect the smallest incubated BSA concentration of 2.5 mg/mL, corresponding to a film layer of a few tens of nm, with all the antenna samples used in this work. This detection limit is 16 times less than the HSA concentration in human blood [37]. Furthermore, the cost-competitive fabrication of Ge antennas, their intrinsic small footprint and its potential integration with microfluidic/nanofluidic devices could enable the parallel analysis (multiplexing) of the biological samples on-site [46–48].

4. Conclusions

In summary, we presented THz biochip sensors consisting of highly n-doped Ge plasmonic THz microstructures based on Si/SOI substrates, entirely realized in an industry-standard CMOS foundry pilot line. We demonstrated that different deposited BSA concentrations, leading to very thin (tens of nm) protein layers, can be quantitatively sensed using THz-TDS. Indeed, Ge-based antenna array sensitivity of up to ~6 GHz/(mg/mL) has been obtained, which is fourfold larger than those reported on metal-based metamaterial sensing.

From a biomedical point of view, the results here reported represent an important step forward in the integration of plasmonic-based platforms with the current microelectronics ecosystem. By combining surface biofunctionalization for affinity capturing of target proteins, this CMOS-compatible platform can be further enhanced for specificity and sensitivity of serum biomarkers detection for personalized point-of-care medical applications.

Disclosures. The authors declare that there are no conflicts of interest related to this article.

Data availability. Data underlying the results presented in this paper are not publicly available at this time but may be obtained from the authors upon reasonable request.

References

1. A. Berrier, P. Albella, M. A. Poyli, R. Ulbricht, M. Bonn, J. Aizpurua, and J. G. Rivas, "Detection of deep-subwavelength dielectric layers at terahertz frequencies using semiconductor plasmonic resonators," Opt. Express **20**(5), 5052 (2012).
2. A. Bandyopadhyay and A. Sengupta, "A Review of the Concept, Applications and Implementation Issues of Terahertz Spectral Imaging Technique," IETE Technical Review **39**(2), 471–489 (2022).
3. J. Uddin, eds., *Terahertz Spectroscopy - A Cutting Edge Technology* (InTech, 2017).
4. S. Wang, L. Xia, H. Mao, X. Jiang, S. Yan, H. Wang, D. Wei, H. Cui, and C. Du, "Terahertz biosensing based on a polarization-insensitive metamaterial," IEEE Photonics Technol. Lett. **39**, 1 (2016).
5. X. Huang, Y. Jiang, Y. Shang, H. Yu, and L. Sun, "A CMOS THz-sensing system towards label-free DNA sequencing," in *2015 IEEE 11th International Conference on ASIC (ASICON)* (IEEE, 2015), pp. 1–4.
6. X. Wu, L. Wang, Y. Peng, F. Wu, J. Cao, X. Chen, W. Wu, H. Yang, M. Xing, Y. Zhu, Y. Shi, and S. Zhuang, "Quantitative analysis of direct oral anticoagulant rivaroxaban by terahertz spectroscopy," Analyst **145**(11), 3909–3915 (2020).
7. L. Liu, T. Li, Z. Liu, F. Fan, H. Yuan, Z. Zhang, S. Chang, and X. Zhang, "Terahertz polarization sensing based on metasurface microsensor display anti-proliferation of tumor cells with aspirin," Biomed. Opt. Express **11**(5), 2416 (2020).
8. S. Lin, Y. Wang, Z. Peng, Z. Chen, and F. Hu, "Detection of cancer biomarkers CA125 and CA199 via terahertz metasurface immunosensor," Talanta **248**, 123628 (2022).
9. T. Mancini, R. Mosetti, A. Marcelli, M. Petrarca, S. Lupi, and A. D'Arco, "Terahertz Spectroscopic Analysis in Protein Dynamics: Current Status," Radiation **2**(1), 100–123 (2022).
10. S. Ebbinghaus, S. J. Kim, M. Heyden, X. Yu, U. Heugen, M. Gruebele, D. M. Leitner, and M. Havenith, "An extended dynamical hydration shell around proteins," Proc. Natl. Acad. Sci. **104**(52), 20749–20752 (2007).
11. N. L. Henry and D. F. Hayes, "Cancer biomarkers," Mol. Oncol. **6**(2), 140–146 (2012).
12. G. M. Vita, G. De Simone, E. De Marinis, C. Nervi, P. Ascenzi, and A. di Masi, "Serum albumin and nucleic acids biodistribution: From molecular aspects to biotechnological applications," IUBMB Life iub.2653 (2022).
13. N. Bellassai, R. D'Agata, V. Jungbluth, and G. Spoto, "Surface Plasmon Resonance for Biomarker Detection: Advances in Non-invasive Cancer Diagnosis," Front. Chem. **7**, 570 (2019).
14. L. Leboffe, A. di Masi, F. Polticelli, V. Trezza, and P. Ascenzi, "Structural Basis of Drug Recognition by Human Serum Albumin," Curr. Med. Chem. **27**(30), 4907–4931 (2020).
15. L. Zhu, K. Wang, J. Cui, H. Liu, X. Bu, H. Ma, W. Wang, H. Gong, C. Lausted, L. Hood, G. Yang, and Z. Hu, "Label-Free Quantitative Detection of Tumor-Derived Exosomes through Surface Plasmon Resonance Imaging," Anal. Chem. **86**(17), 8857–8864 (2014).
16. N. Akter, M. M. Hasan, and N. Pala, "A Review of THz Technologies for Rapid Sensing and Detection of Viruses including SARS-CoV-2," Biosensors **11**(10), 349 (2021).
17. A. di Masi, V. Trezza, L. Leboffe, and P. Ascenzi, "Human plasma lipocalins and serum albumin: Plasma alternative carriers?" J. Controlled Release **228**, 191–205 (2016).

18. L. Sun, L. Zhao, and R.-Y. Peng, "Research progress in the effects of terahertz waves on biomacromolecules," Mil. Med. Res. **8**(1), 28 (2021).

19. S. Law, R. Liu, and D. Wasserman, "Doped semiconductors with band-edge plasma frequencies," J. Vac. Sci. Technol., B: Nanotechnol. Microelectron.: Mater., Process., Meas., Phenom. **32**(5), 052601 (2014).

20. L. Baldassarre, E. Sakat, J. Frigerio, A. Samarelli, K. Gallacher, E. Calandrini, G. Isella, D. J. Paul, M. Ortolani, and P. Biagioni, "Midinfrared Plasmon-Enhanced Spectroscopy with Germanium Antennas on Silicon Substrates," Nano Lett. **15**(11), 7225–7231 (2015).

21. D.-K. Lee, J.-H. Kang, J.-S. Lee, H.-S. Kim, C. Kim, J. Hun Kim, T. Lee, J.-H. Son, Q.-H. Park, and M. Seo, "Highly sensitive and selective sugar detection by terahertz nano-antennas," Sci. Rep. **5**(1), 15459 (2015).

22. A. Ahmadivand, B. Gerislioglu, P. Manickam, A. Kaushik, S. Bhansali, M. Nair, and N. Pala, "Rapid Detection of Infectious Envelope Proteins by Magnetoplasmonic Toroidal Metasensors," ACS Sens. **2**(9), 1359–1368 (2017).

23. T. Wang, S. Shen, J. Liu, Y. Zhang, and Z. Han, "Experimental realization of perfect terahertz plasmonic absorbers using highly doped silicon substrate and CMOS-compatible techniques," Opt. Mater. Express **6**(2), 523 (2016).

24. Y. Liu, T. Sun, Y. Xu, X. Wu, Z. Bai, Y. Sun, H. Li, H. Zhang, K. Chen, C. Ruan, Y. Sun, Y. Hu, W. Zhao, T. Nie, and L. Wen, "Active tunable THz metamaterial array implemented in CMOS technology," J. Phys. D: Appl. Phys. **54**(8), 085107 (2021).

25. I. A. Fischer, M. Brehm, M. De Seta, G. Isella, D. J. Paul, M. Virgilio, and G. Capellini, "On-chip infrared photonics with Si-Ge-heterostructures: What is next?" APL Photonics **7**(5), 050901 (2022).

26. M. Bettenhausen, F. Römer, B. Witzigmann, J. Flesch, R. Kurre, S. Korneev, J. Piehler, C. You, M. Kazmierczak, S. Guha, G. Capellini, and T. Schröder, "Germanium Plasmon Enhanced Resonators for Label-Free Terahertz Protein Sensing," Frequenz **72**(3-4), 113–122 (2018).

27. C. A. Chavarin, E. Hardt, S. Gruessing, O. Skibitzki, I. Costina, D. Spirito, W. Seifert, W. Klesse, C. L. Manganelli, C. You, J. Flesch, J. Piehler, M. Missori, L. Baldassarre, B. Witzigmann, and G. Capellini, "n-type Ge/Si antennas for THz sensing," Opt. Express **29**(5), 7680 (2021).

28. A. Berrier, M. C. Schaafsma, G. Nonglaton, J. Bergquist, and J. G. Rivas, "Selective detection of bacterial layers with terahertz plasmonic antennas," Biomed. Opt. Express **3**(11), 2937 (2012).

29. S. Di Bella, A. di Masi, S. Turla, P. Ascenzi, T. Gouliouris, and N. Petrosillo, "The Protective Role of Albumin in *Clostridium difficile* Infection: A Step Toward Solving the Puzzle," Infect. Control Hosp. Epidemiol. **36**(12), 1478–1480 (2015).

30. S. Di Bella, P. Ascenzi, S. Siarakas, N. Petrosillo, and A. di Masi, "Clostridium difficile Toxins A and B: Insights into Pathogenic Properties and Extraintestinal Effects," Toxins **8**(5), 134 (2016).

31. A. di Masi, L. Leboffe, F. Polticelli, F. Tonon, C. Zennaro, M. Caterino, P. Stano, S. Fischer, M. Hägele, M. Müller, A. Kleger, P. Papatheodorou, G. Nocca, A. Arcovito, A. Gori, M. Ruoppolo, H. Barth, N. Petrosillo, P. Ascenzi, and S. Di Bella, "Human Serum Albumin Is an Essential Component of the Host Defense Mechanism Against Clostridium difficile Intoxication," J. Infect. Dis. **218**(9), 1424–1435 (2018).

32. S. Austermeier, M. Pekmezović, P. Porschitz, S. Lee, N. Kichik, D. L. Moyes, J. Ho, N. K. Kotowicz, J. R. Naglik, B. Hube, and M. S. Gresnigt, "Albumin Neutralizes Hydrophobic Toxins and Modulates *Candida albicans* Pathogenicity," mBio **12**(3), e00531 (2021).

33. S. Gruessing, B. Witzigmann, F. Römer, G. Capellini, C. C. Alvarado, W. M. Klesse, E. Hardt, J. Piehler, C. You, and J. Flesch, "Modeling of plasmonic semiconductor THz antennas in square and hexagonal array arrangements," in *Terahertz, RF, Millimeter, and Submillimeter-Wave Technology and Applications XIII*, L. P. Sadwick and T. Yang, eds. (SPIE, 2020), p. 76.

34. G. De Simone, A. di Masi, and P. Ascenzi, "Serum Albumin: A Multifaced Enzyme," Int. J. Mol. Sci. **22**(18), 10086 (2021).

35. A. Bujacz, "Structures of bovine, equine and leporine serum albumin," Acta Crystallogr D Biol Crystallogr **68**(10), 1278–1289 (2012).

36. G. Fanali, A. di Masi, V. Trezza, M. Marino, M. Fasano, and P. Ascenzi, "Human serum albumin: From bench to bedside," Mol. Aspects Med. **33**(3), 209–290 (2012).

37. N. Hassler, D. Baurecht, G. Reiter, and U. P. Fringeli, "In Situ FTIR ATR Spectroscopic Study of the Interaction of Immobilized Human Serum Albumin with Cholate in Aqueous Environment," J. Phys. Chem. C **115**(4), 1064–1072 (2011).

38. G. Güler, M. M. Vorob'ev, V. Vogel, and W. Mäntele, "Proteolytically-induced changes of secondary structural protein conformation of bovine serum albumin monitored by Fourier transform infrared (FT-IR) and UV-circular dichroism spectroscopy," Spectrochim. Acta, Part A **161**, 8–18 (2016).

39. A.-H. Chiou, J.-L. Wei, and S.-H. Chen, "Ag-Functionalized Si Nanowire Arrays Aligned Vertically for SERS Detection of Captured Heavy Metal Ions by BSA," Coatings **11**(6), 685 (2021).

40. F. Ahmad, Y. Zhou, Z. Ling, Q. Xiang, and X. Zhou, "Systematic elucidation of interactive unfolding and corona formation of bovine serum albumin with cobalt ferrite nanoparticles," RSC Adv. **6**(42), 35719–35730 (2016).

41. R. Wang and Y. Wang, "Fourier Transform Infrared Spectroscopy in Oral Cancer Diagnosis," Int. J. Mol. Sci. **22**(3), 1206 (2021).

42. M. Hassan, X. Tan, E. Welle, and I. Ilev, "Fiber-optic Fourier transform infrared spectroscopy for remote label-free sensing of medical device surface contamination," Rev. Sci. Instrum. **84**(5), 053101 (2013).

43. M. Seo and H. Park, "Terahertz Biochemical Molecule-Specific Sensors," Adv. Opt. Mater. **8**(3), 1900662 (2020).

44. Dr. M. Öri, "Menlo Systems," https://www.menlosystems.com/products/thz-time-domain-solutions/terasmart-terahertz-spectrometer/.

45. O. Krivosudský, P. Dráber, and M. Cifra, "Resolving controversy of unusually high refractive index of a tubulin," EPL **117**(3), 38003 (2017).

46. A. Azzouz, L. Hejji, K.-H. Kim, D. Kukkar, B. Souhail, N. Bhardwaj, R. J. C. Brown, and W. Zhang, "Advances in surface plasmon resonance–based biosensor technologies for cancer biomarker detection," Biosens. Bioelectron. **197**, 113767 (2022).

47. Z. Fattahi, A. Y. Khosroushahi, and M. Hasanzadeh, "Recent progress on developing of plasmon biosensing of tumor biomarkers: Efficient method towards early stage recognition of cancer," Biomed. Pharmacother. **132**, 110850 (2020).

48. A. Gharatape and A. Yari Khosroushahi, "Optical Biomarker-based Biosensors for Cancer/Infectious Disease Medical Diagnoses," Appl. Immunohistochem. Mol. Morphol. **27**(4), 278–286 (2019).